# LETTER

# Observation of three–component fermions in the topological semimetal molybdenum phosphide

B. Q. Lv[1,2*], Z.-L. Feng[1,2*], Q.-N. Xu[1,2*], X. Gao[1,2], J.-Z. Ma[1,2], L.-Y. Kong[1,2], P. Richard[1,2,3], Y.-B. Huang[4], V. N. Strocov[5], C. Fang[1], H.-M. Weng[1,3], Y.-G. Shi[1], T. Qian[1,3] & H. Ding[1,2,3]

**In quantum field theory, Lorentz invariance leads to three types of fermion—Dirac, Weyl and Majorana. Although the existence of Weyl and Majorana fermions as elementary particles in high-energy physics is debated, all three types of fermion have been proposed to exist as low-energy, long-wavelength quasiparticle excitations in condensed-matter systems[1–12]. The existence of Dirac and Weyl fermions in condensed-matter systems has been confirmed experimentally[13–18], and that of Majorana fermions is supported by various experiments[19,20]. However, in condensed-matter systems, fermions in crystals are constrained by the symmetries of the 230 crystal space groups rather than by Lorentz invariance, giving rise to the possibility of finding other types of fermionic excitation that have no counterparts in high-energy physics[21–29]. Here we use angle-resolved photoemission spectroscopy to demonstrate the existence of a triply degenerate point in the electronic structure of crystalline molybdenum phosphide. Quasiparticle excitations near a triply degenerate point are three-component fermions, beyond the conventional Dirac–Weyl–Majorana classification, which attributes Dirac and Weyl fermions to four- and two-fold degenerate points, respectively. We also observe pairs of Weyl points in the bulk electronic structure of the crystal that coexist with the three-component fermions. This material thus represents a platform for studying the interplay between different types of fermions. Our experimental discovery opens up a way of exploring the new physics of unconventional fermions in condensed-matter systems.**

All fermions have half-integer spin $S = n + 1/2$, where $n$ is an integer, leading to an even $(2S+1)$-fold degeneracy in the presence of Lorentz invariance, which is incompatible with three-fold degeneracy. However, three-fold degeneracy can be protected in a lattice, either by symmorphic rotation combined with mirror symmetries[21,24–29] or by non-symmorphic symmetries[23]. In either case, the three-component fermions conceptually lie between Weyl (two-component) fermions and Dirac (four-component) fermions (Fig. 1a), but have distinct properties, including unique surface states and transport properties[23,26,27].

First-principles calculations have predicted that the electronic structures of several materials with tungsten carbide structure host triply degenerate points[26–29]. We fabricated single crystals of one such material—molybdenum phosphide (MoP). By investigating the electronic structure of MoP with angle-resolved photoemission spectroscopy (ARPES), here we demonstrate the existence of three-component fermions in this system.

The crystal structure of MoP is characterized by the symmorphic space group $P\bar{6}m2$ (number 187). Within the lattice, molybdenum and phosphorus atoms are located at the 1$d$ (1/3, 2/3, 1/2) and 1$a$ (0, 0, 0) Wyckoff positions, respectively. The crystal structure includes the rotational symmetry $C_{3z}$ and the mirror symmetries $M_y$ and $M_z$, as illustrated in Fig. 1b, c. As discussed below, these crystal symmetries are crucial to protecting the triply degenerate points.

A*b initio* calculations show a band inversion between the $d_{z^2}$ and $e_g$ states of molybdenum at the A point of the Brillouin zone, leading to a band crossing along Γ–A. Without spin–orbit coupling (SOC), the crossing bands are a non-degenerate $d_{z^2}$ orbital band and a doubly degenerate band composed of the $e_g$ ($d_{xy}$ and $d_{x^2-y^2}$) orbitals (Fig. 1e). The triply degenerate crossing is protected by the $C_{3z}$ symmetry, similarly to the Dirac semimetals Na$_3$Bi (ref. 5) and Cd$_3$As$_2$ (ref. 7). When SOC is considered, the bands along Γ–A reconstruct into two non-degenerate $|J_z| = 3/2$ bands and two doubly degenerate $|J_z| = 1/2$ bands, owing to the $M_y$ mirror symmetry (where $J_z$ is the projection of total angular momentum along the $z$ direction). The crossing points of the bands with different $|J_z|$ are protected by the $C_{3z}$ symmetry, leading to four triply degenerate points along the Γ–A line (Fig. 1f). Theory predicts two types of triply degenerate point, which differ in their topology, being connected by either one (type A) or four (type B) nodal lines[21,25,27,29]. In MoP, the triply degenerate points belong to the type-A class, and each pair of triply degenerate points ({TP1, TP2} or {TP3, TP4}) is interconnected by one doubly degenerate nodal line along Γ–A (Fig. 1f).

We first perform core-level photoemission measurements, which confirm the chemical composition of MoP (Fig. 2a). Next we investigate the electronic structure of MoP with systematic ARPES measurements on the (100) and (001) surfaces. Although the mirror-like (100) and (001) surfaces were obtained by cleaving, the data recorded with vacuum ultraviolet light are not clear for the (001) surface and do not show any features for the (100) surface. By contrast, the data obtained using soft X-rays clearly exhibit band dispersions and Fermi surfaces on both cleaved surfaces. The photoelectrons excited by soft X-rays have a much longer escape depth, which not only improves the bulk sensitivity of the ARPES measurements substantially, but also increases the intrinsic momentum resolution normal to the surface, as a result of the Heisenberg uncertainty principle[30], thus facilitating the extraction of the electronic structures of three-dimensional systems such as MoP.

Figure 2 displays the overall electronic structure in the three-dimensional Brillouin zone recorded on the (100) and (001) surfaces. The experimental Fermi surfaces in the high-symmetry planes (Fig. 2c, d, h) and the band dispersions along the high-symmetry lines (Fig. 2f, j) are consistent with the calculated bulk electronic structure. In addition, we observe small patches at the Γ (Fig. 2d) and A (Fig. 2h) points, which are attributed to a broadening along the momentum perpendicular to the sample surface ($k_z$) of the small electronic-like Fermi surfaces that are located between Γ and A (Fig. 2b). The consistency between experiments and calculations gives us confidence to search for the triply degenerate points that are predicted theoretically.

[1]Beijing National Laboratory for Condensed Matter Physics and Institute of Physics, Chinese Academy of Sciences, Beijing 100190, China. [2]University of Chinese Academy of Sciences, Beijing 100049, China. [3]Collaborative Innovation Center of Quantum Matter, Beijing, China. [4]Shanghai Synchrotron Radiation Facility, Shanghai Institute of Applied Physics, Chinese Academy of Sciences, Shanghai 201204, China. [5]Paul Scherrer Institute, Swiss Light Source, CH-5232 Villigen, Switzerland.
*These authors contributed equally to this work.
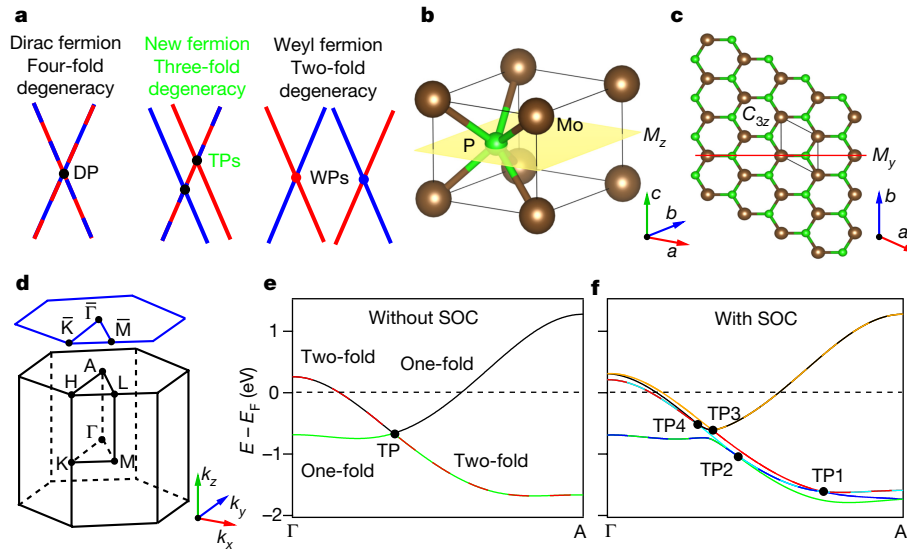
**Figure 1 | Crystal structure and band structure of MoP along the Γ–A line in the Brillouin zone. a**, Schematics of Dirac and Weyl fermions, and our newly discovered fermion, which have band crossing points with four- (Dirac point, DP), two- (Weyl point, WP) and three-fold (triply degenerate point, TP) degeneracies, respectively. **b**, Three-dimensional crystal structure of MoP. The yellow plane indicates the mirror plane $M_z$. **c**, Top view of the lattice showing the $C_{3z}$ rotation symmetry with respect to molybdenum (brown spheres) or phosphide (green spheres) and the $M_y$ mirror plane (horizontal red line). **d**, Three-dimensional bulk Brillouin zone (black) and the projected (001) surface Brillouin zone (blue), with high-symmetry points indicated. **e**, **f**, Calculated band structures along Γ–A (in terms of the energy $E$ relative to the Fermi energy $E_F$) without (**e**) and with (**f**) SOC. The filled circles at the crossing points indicate the triply degenerate points. The curves with mixed colours represent doubly degenerate bands and those with uniform colour represent non-degenerate bands.
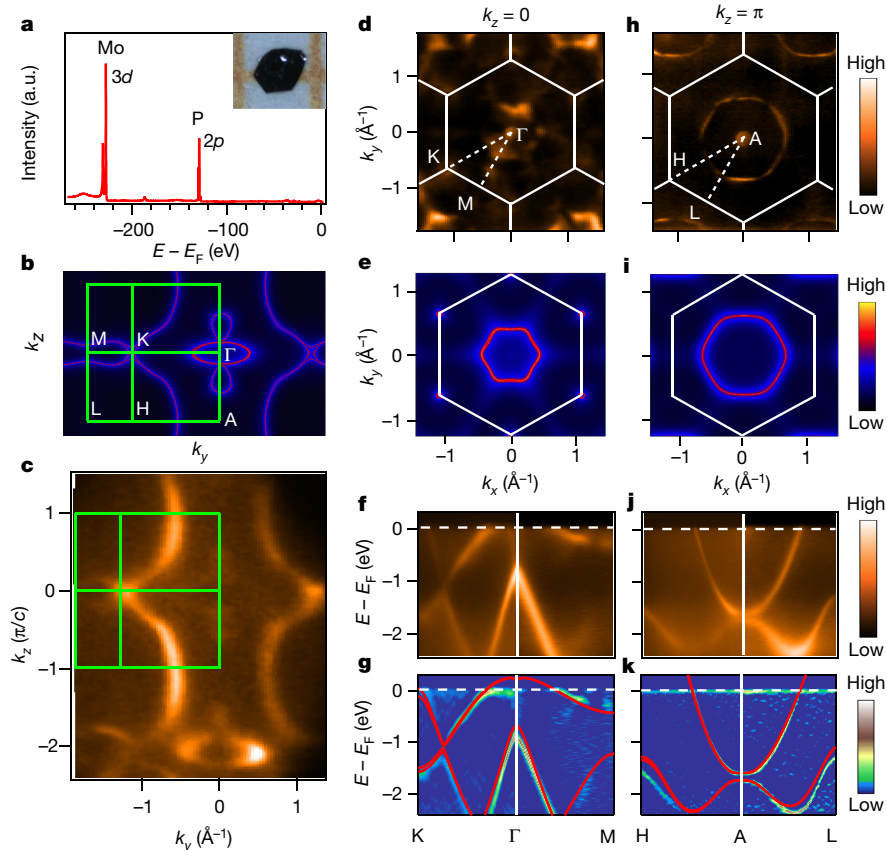


**Figure 2 | Overall electronic structure of MoP in the three-dimensional Brillouin zone of the bulk. a**, Core-level photoemission spectrum showing characteristic molybdenum (Mo) $3d$ and phosphorus (P) $2p$ peaks. The inset shows a typical single crystal of MoP. a.u., arbitrary units. **b**, **c**, Calculated (**b**) and experimental (**c**) intensity plots at $E_F$, showing Fermi surfaces in the $k_x = 0$ plane. The green boxes indicate the Brillouin zone boundary in the $k_x = 0$ plane. **d**, **e**, Experimental (**d**) and calculated (**e**) intensity plots at $E_F$, showing Fermi surfaces in the $k_z = 0$ plane. The white hexagons indicate the Brillouin zone boundary in the $k_z = 0$ plane. **f**, **g**, ARPES (**f**) and curvature intensity (**g**) plots, showing band dispersions along K–Γ–M. For comparison, the calculated band structure along K–Γ–M is superposed on the experimental data in **g**. **h**–**k**, Same as **d**–**g**, but in the $k_z = \pi$ plane. The data in **c** were recorded on the (100) cleavage surface; those in **d**, **f**, **h** and **j** were obtained on the (001) cleavage surface.
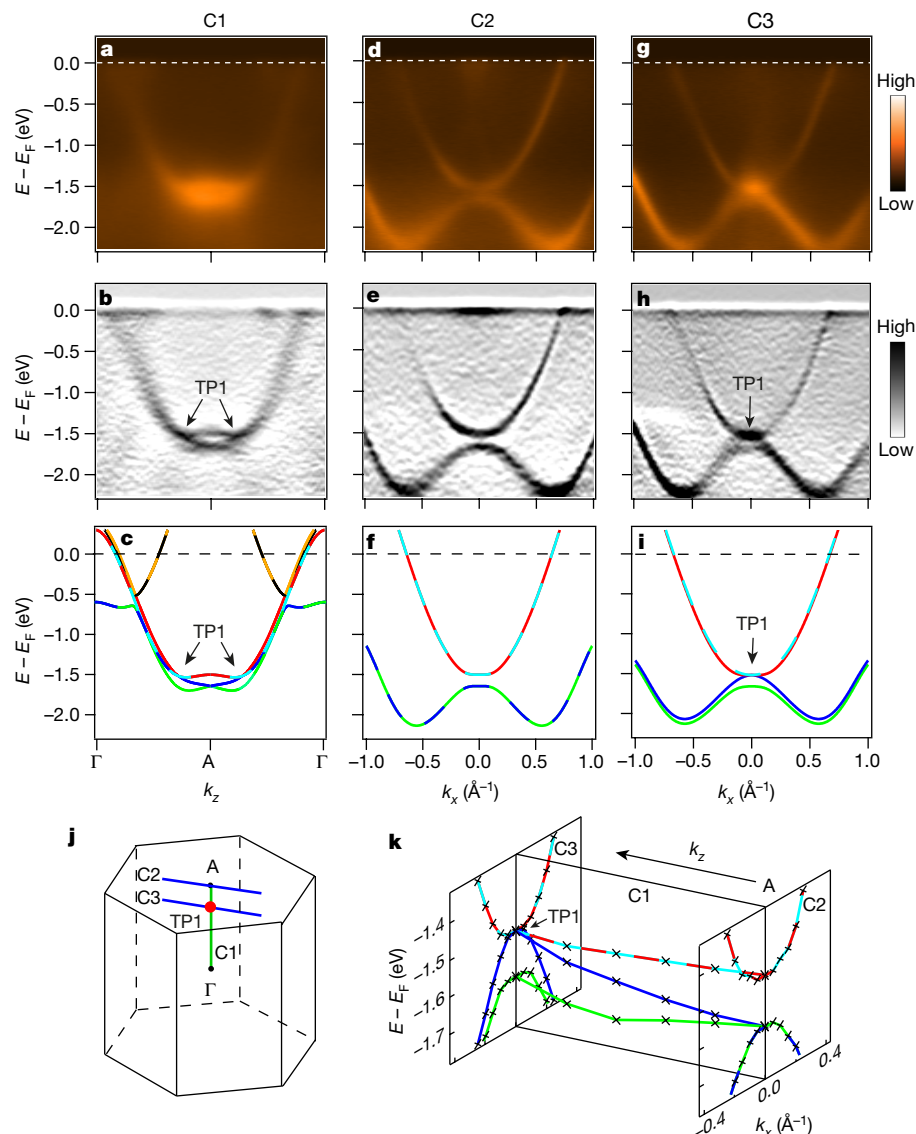
**Figure 3 | Electronic structure near TP1. a–c,** ARPES (**a**) and curvature (**b**) intensity plots and the calculated band structure (**c**) along C1 (green line in **j**). **d–i,** Same as **a–c,** but along C2 (**d–f**) or C3 (**g–i**) (blue lines in **j**). The curves in **c, f,** and **i** are coloured as in Fig. 1d, e. **j,** Schematic of the bulk Brillouin zone, including the lines C1, C2 and C3, which indicate the momentum locations of the cuts in **a–c, d–f** and **g–i,** respectively. **k,** Three-dimensional plot of the band dispersions along C1, C2 and C3. The symbols represent the band dispersions that were extracted by tracking the peak positions of the curvature intensity data in **b, e** and **h**. The data along C1 were recorded on the (100) cleavage surface; those along C2 and C3 were obtained on the (001) cleavage surface.

Next we demonstrate the existence of triply degenerate points in MoP by using high-precision measurements of the band dispersions. The plot of ARPES intensity (Fig. 3a) displays an electron-like band dispersion along Γ–A. The details of the band structure around A are resolved in the corresponding curvature intensity plot (Fig. 3b). We observe two band bottoms that are doubly degenerate at the time-reversal-invariant momentum A. Upon dispersing towards Γ, the upper band remains doubly degenerate while the lower band splits into two non-degenerate bands. One of the non-degenerate bands crosses the doubly degenerate band, forming one triply degenerate point at $k_z = 0.75\pi$ on the Γ–A line. The observation agrees well with the calculated band structure around A shown in Fig. 3c, in which the triply degenerate point that we identified corresponds to TP1 in the calculations.

To further resolve the band structure related to TP1, we measured band dispersions along the in-plane momentum parallel to Γ–M ($k_x$) at $k_z = \pi$ and $k_z = 0.75\pi$. The experimental band dispersions (Fig. 3d, e) at $k_z = \pi$ (C2 in Fig. 3j) exhibit one electron-like band and one 'W'-shaped band, with an energy gap of 0.1 eV at A, consistent with the calculation (Fig. 3f). Note that all of the bands along A–L, which are protected by

the $D_2$ little-group symmetry, are doubly degenerate. Upon sliding the cut to $k_z = 0.75\pi$ (C3 in Fig. 3j), which intersects TP1, the 'W'-shaped band splits and its upper branch touches the electron-like band (Fig. 3h). This observation also agrees well with the calculation (Fig. 3i). We show in Fig. 3k a three-dimensional plot of the band dispersions extracted from the experimental results.

In addition to the triply degenerate points, we discovered the existence of Weyl points in the electronic structure of MoP. Our calculations show a band inversion at the K point in the Brillouin zone. Without SOC, the band inversion forms a nodal ring centred at K in the $k_z = 0$ mirror plane (Fig. 4a). With SOC included, the lack of inversion symmetry leads to Rashba-like spin splitting. The nodal rings in the mirror plane are fully gapped, and pairs of Weyl points appear in the Γ–K direction off the plane (Fig. 4a). All of the Weyl points can be related to each other by the $D_{3h}$ crystal symmetry and are therefore located at the same energy. The calculated electronic structure of MoP is similar to that of ZrTe (ref. 28), except that the Weyl points of MoP are located at energies $E$ of −1.1 eV, relative to the Fermi energy $E_F$, whereas those of ZrTe are at 0.05 eV.
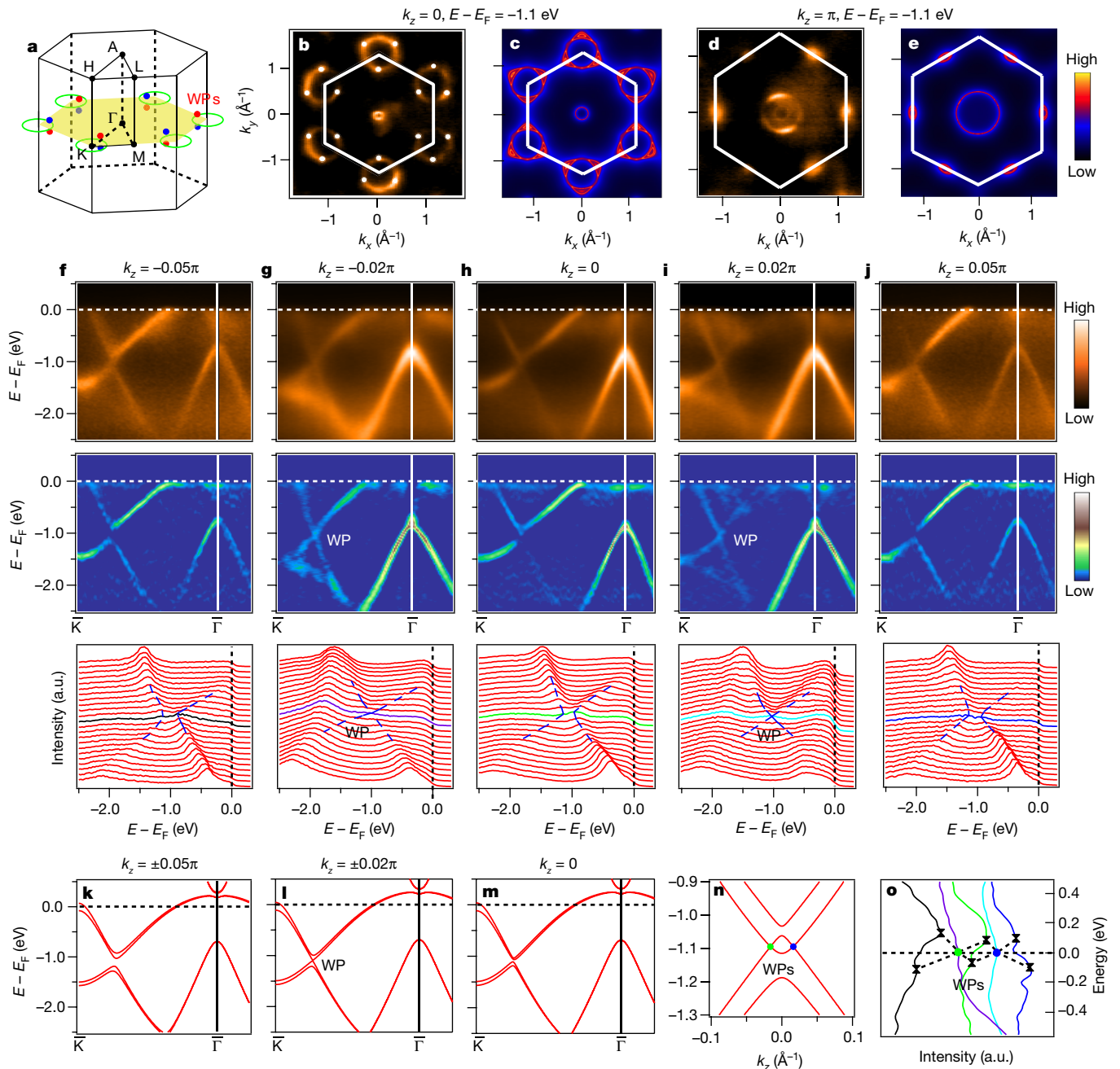
**Figure 4 | Electronic structure near the Weyl points. a**, Three-dimensional bulk Brillouin zone. Nodal lines are evident in the $k_z = 0$ mirror plane without SOC, whereas Weyl points appear off the plane with SOC. **b, c**, Experimental (**b**) and calculated (**c**) intensity plots at $E − E_F = −1.1$ eV in the $k_z = 0$ plane. White dots in **b** indicate the projected locations of the Weyl points. **d, e**, Same as **b, c**, but in the $k_z = \pi$ plane. **f**, ARPES (top) and curvature (middle) intensity plots along $\overline{\Gamma}–\overline{K}$ and the energy distribution curves near the Weyl point (WP; bottom) at $k_z = −0.05\pi$. The blue dashed lines (bottom) highlight the band dispersions. **g–j**, Same as **f**, but at $k_z = −0.02\pi$ (**g**), $k_z = 0$ (**h**), $k_z = 0.02\pi$ (**i**)

and $k_z = 0.05\pi$ (**j**). **k–m**, Calculated band structures along $\overline{\Gamma}–\overline{K}$ at $k_z = \pm0.05\pi$ (**k**), $k_z = \pm0.02\pi$ (**l**) and $k_z = 0$ (**m**). **n**, Calculated band structure along $k_z$ through one pair of Weyl points (with opposite chiral charge; green and blue filled circles). **o**, Energy distribution curves along $k_z$ through one pair of Weyl points, colour-coded to match those in the bottom panels of **f–j**. Zero energy in **o** is set to the energy of the Weyl points. The triangles, which are connected by the dashed lines, highlight the band dispersions near the Weyl points. All data were recorded on the (001) cleavage surface.

Figure 4b clearly shows a ring around the K point at −1.1 eV in the $k_z = 0$ plane, which is related to the nodal ring that was calculated in the absence of SOC. To confirm the existence of Weyl points, we measured the band dispersions along $\overline{\Gamma}–\overline{K}$ at different $k_z$. The bands along $\overline{\Gamma}–\overline{K}$ form a small gap at $0.75\overline{\Gamma K}$ at $k_z = 0$ (Fig. 4h). The gap closes at $k_z = \pm0.02\pi$ (Fig. 4g, i) and reopens at $k_z = \pm0.05\pi$ (Fig. 4f, j). These results clearly indicate the existence of Weyl points along the $\Gamma$–K direction at $k_z = \pm0.02\pi$, consistent with the theoretical prediction (Fig. 4k–n). The results show that the velocities of the bands crossing

at the Weyl points have opposite sign along the in-plane momentum parallel to $\Gamma$–K ($k_y$) and $k_z$. Given that the velocities must have opposite sign along $k_x$, the Weyl points in MoP belong to the type-I class[12].

One hallmark of topological semimetals is the surface states that are associated with the nodal points. Because all of the predicted triply degenerate points in MoP are located on the $\Gamma$–A line, they are projected onto the same $\overline{\Gamma}$ point in the (001) surface Brillouin zone. The projected triply degenerate points and the associated surface states are superposed by the projection of continuous bulk states onto the

(001) surface; the surface states do not show up on the (001) surface. The Weyl points with opposite chiral charge are projected on top of one another on the (001) surface, the surface states of which are not topologically protected. Consequently, the arc that connects the projections becomes a closed loop and may continuously shrink to a point, which is equivalent to there being no arc. Therefore, no signatures of surface states associated with the triply degenerate points and Weyl points are identified on the (001) surface. In contrast, topologically protected surface states are expected on the (100) surface[26–28]. However, we observed only bulk states for the (100) surface using bulk-sensitive soft X-rays, and no feature was detected using surface-sensitive vacuum ultraviolet light. Scanning tunnelling microscopy measurements (not shown) reveal that the termination layer on the (100) surface is rather disordered, even though the cleavage surface is mirror-like. We therefore speculate that disorder disrupts the surface states that are localized on the termination layer.

Our ARPES results provide an observation of triply degenerate points in the electronic structure of crystalline MoP, demonstrating the existence of three-component fermions. The triply degenerate points in MoP are protected by rotation and mirror symmetries. The breakdown of these symmetries splits the triply degenerate points into either Weyl points or nodal lines, depending on the nature of the symmetry-breaking perturbation. We therefore expect that, if the Fermi energy is near a triply degenerate point, an external magnetic field would lead to anisotropic quantum phenomena, such as the anisotropic chiral anomaly. Another notable feature of the electronic structure is that each triply degenerate point is tied to one doubly degenerate nodal line, leading to Fermi surface touching near the triply degenerate point for arbitrary $E_F$. This Fermi surface touching may cause a 'magnetic breakdown' in quantum oscillations, whereby the semi-classical orbits become undefined as a result of tunnelling between the touching Fermi surfaces. Moreover, these touching Fermi surfaces have a unique spin texture, with the spin winding around exactly twice around along any horizontal loop around $k_z$ on the Fermi surface, and the two Fermi surfaces having opposite winding[26]. Finally, the coexisting three-component fermions and Weyl fermions that are located at different momenta could couple to each other through electron interactions, which would provide a platform for studying the interplay between different types of fermions. With the discovery of three-component fermions in MoP, our work enables further identification of topological semimetals in the tungsten carbide family with triply degenerate points, which are ideal materials for studying unusual properties related to new fermions. Beyond three-component fermions, theories predict a tremendous number of materials that host other types of unconventional fermion. The discovery of exotic quantum phenomena in new fermion systems could pave the way for new applications.

1. Castro Neto, A. H. *et al.* The electronic properties of graphene. *Rev. Mod. Phys.* **81,** 109–162 (2009).
2. Fu, L. & Kane, C. L. Superconducting proximity effect and Majorana fermions at the surface of a topological insulator. *Phys. Rev. Lett.* **100,** 096407 (2008).
3. Lutchyn, R. M., Sau, J. D. & Das Sarma, S. Majorana fermions and a topological phase transition in semiconductor-superconductor heterostructures. *Phys. Rev. Lett.* **105,** 077001 (2010).
4. Oreg, Y., Refael, G. & Von Oppen, F. Helical liquids and Majorana bound states in quantum wires. *Phys. Rev. Lett.* **105,** 177002 (2010).
5. Wang, Z. *et al.* Dirac semimetal and topological phase transitions in $A_3Bi$ (A = Na, K, Rb). *Phys. Rev. B* **85,** 195320 (2012).
6. Young, S. M. *et al.* Dirac semimetal in three dimensions. *Phys. Rev. Lett.* **108,** 140405 (2012).
7. Wang, Z., Weng, H., Wu, Q., Dai, X. & Fang, Z. Three-dimensional Dirac semimetal and quantum transport in $Cd_3As_2$. *Phys. Rev. B* **88,** 125427 (2013).
8. Wan, X., Turner, A. M., Vishwanath, A. & Savrasov, S. Y. Topological semimetal and Fermi-arc surface states in the electronic structure of pyrochlore iridates. *Phys. Rev. B* **83,** 205101 (2011).
9. Xu, G., Weng, H., Wang, Z., Dai, X. & Fang, Z. Chern semimetal and the quantized anomalous Hall effect in $HgCr_2Se_4$. *Phys. Rev. Lett.* **107,** 186806 (2011).
10. Weng, H., Fang, C., Fang, Z., Bernevig, B. A. & Dai, X. Weyl semimetal phase in noncentrosymmetric transition-metal monophosphides. *Phys. Rev. X* **5,** 011029 (2015).
11. Huang, S. M. *et al.* A Weyl Fermion semimetal with surface Fermi arcs in the transition metal monopnictide TaAs class. *Nat. Commun.* **6,** 7373 (2015).
12. Soluyanov, A. A. *et al.* Type-II Weyl semimetals. *Nature* **527,** 495–498 (2015).
13. Liu, Z. K. *et al.* A stable three-dimensional topological Dirac semimetal $Cd_3As_2$. *Nat. Mater.* **13,** 677–681 (2014).
14. Liu, Z. K. *et al.* Discovery of a three-dimensional topological Dirac semimetal. $Na_3Bi$. *Science* **343,** 864–867 (2014).
15. Lv, B. Q. *et al.* Experimental discovery of Weyl semimetal TaAs. *Phys. Rev. X* **5,** 031013 (2015).
16. Xu, S.-Y. *et al.* Discovery of a Weyl fermion semimetal and topological Fermi arcs. *Science* **349,** 613–617 (2015).
17. Lv, B. Q. *et al.* Observation of Weyl nodes in TaAs. *Nat. Phys.* **11,** 724–727 (2015).
18. Yang, L. X. *et al.* Weyl semimetal phase in the non-centrosymmetric compound TaAs. *Nat. Phys.* **11,** 728–732 (2015).
19. Mourik, V. *et al.* Signatures of Majorana fermions in hybrid superconductor-semiconductor nanowire devices. *Science* **336,** 1003–1007 (2012).
20. Nadj-Perge, S. *et al.* Observation of Majorana fermions in ferromagnetic atomic chains on a superconductor. *Science* **346,** 602–607 (2014).
21. Heikkilä, T. T. & Volovik, G. E. Nexus and Dirac lines in topological materials. *New J. Phys.* **17,** 093019 (2015).
22. Wieder, B. J., Kim, Y., Rappe, A. M. & Kane, C. L. Double Dirac semimetals in three dimensions. *Phys. Rev. Lett.* **116,** 186402 (2016).
23. Bradlyn, B. *et al.* Beyond Dirac and Weyl fermions: unconventional quasiparticles in conventional crystals. *Science* **353,** aaf5037 (2016).
24. Winkler, G. W., Wu, Q., Troyer, M., Krogstrup, P. & Soluyanov, A. A. Topological phases in $InAs_{1−x}Sb_x$: from novel topological semimetal to Majorana wire. *Phys. Rev. Lett.* **117,** 076403 (2016).
25. Hyart, T. & Heikkilä, T. T. Momentum-space structure of surface states in a topological semimetal with a nexus point of Dirac lines. *Phys. Rev. B* **93,** 235147 (2016).
26. Weng, H., Fang, C., Fang, Z. & Dai, X. Topological semimetals with triply degenerate nodal points in θ-phase tantalum nitride. *Phys. Rev. B* **93,** 241202 (2016).
27. Zhu, Z., Winkler, G. W., Wu, Q. S., Li, J. & Soluyanov, A. A. Triple point topological metals. *Phys. Rev. X* **6,** 031003 (2016).
28. Weng, H., Fang, C., Fang, Z. & Dai, X. Co-existence of Weyl fermion and massless triply degenerate nodal points. *Phys. Rev. B* **94,** 165201 (2016).
29. Chang, G. *et al.* New fermions on the line in topological symmorphic metals. Preprint at https://arXiv.org/abs/1605.06831 (2016).
30. Strocov, V. N. *et al.* Three-dimensional electron realm in $VSe_2$ by soft X-ray photoelectron spectroscopy: origin of charge-density waves. *Phys. Rev. Lett.* **109,** 086401 (2012).

**Author Contributions** H.D. and T.Q. conceived the experiments; B.Q.L., X.G. and T.Q. performed the ARPES measurements with assistance from J.-Z.M., L.-Y.K., Y.-B.H. and V.N.S.; Q.-N.X. and H.-M.W. performed the *ab initio* calculations; B.Q.L., T.Q. and H.D. analysed the experimental data; B.Q.L., Q.-N.X. and T.Q. made the figures; T.Q., C.F., H.D., B.Q.L. and P.R. wrote the manuscript; and Z.-L.F. and Y.-G.S. synthesized the single crystals.

**Author Information** Reprints and permissions information is available at www.nature.com/reprints. The authors declare no competing financial interests. Readers are welcome to comment on the online version of the paper. Publisher's note: Springer Nature remains neutral with regard to jurisdictional claims in published maps and institutional affiliations. Correspondence and requests for materials should be addressed to H.D. (dingh@iphy.ac.cn), T.Q. (tqian@iphy.ac.cn) and Y.-G.S. (ygshi@iphy.ac.cn).

## METHODS

**Sample synthesis.** Single crystals of MoP were synthesized via a solid-state reaction with Ge as the flux. Stoichiometric Mo (99.95%) and P (99.999%) were mixed with an appropriate amount of Ge (99.9999%) flux and were placed in an aluminium oxide ampoule. The ampoule was sealed into a Ta tube under Ar atmosphere and then in an evacuated quartz tube. The samples were heated slowly to 1,150 °C and kept at that temperature for 10 h. The samples were then cooled to 1,000 °C over one week. The Ge flux was removed in a centrifuge at 1,000 °C. The areas of the hexagonal surfaces of the single crystals are up to 1 mm$^2$, and the thicknesses of the single crystals are up to 0.2 mm.

**Angle-resolved photoemission spectroscopy.** Soft X-ray ARPES measurements were performed at the 'Dreamline' beamline of the Shanghai Synchrotron Radiation Facility (SSRF) with a Scienta Omicron DA30L analyser, and at the Advanced Resonant Spectroscopies (ADRESS) beamline at the Swiss Light Source (SLS) with a SPECS analyser[31]. The photon energy ranged from 300 eV to 1,000 eV, and the combined (beamline and analyser) experimental energy resolution of the soft X-ray ARPES measurements varied from 40 meV to 100 meV. The angular resolution of the DA30L analyser was 0.1° and that of the SPECS analyser was 0.07°. Fresh surfaces were obtained by cleaving MoP samples *in situ* in a vacuum with a pressure of less than $5 \times 10^{-11}$ torr.

**Band structure calculations.** The first-principles calculations of the electronic band structure were performed using the Vienna *ab initio* simulation package (VASP)[32], with the generalized gradient approximation (GGA) of Perdew–Burke–Ernzerhof (PBE) type[33] used as the exchange-correlation potential. Spin–orbit coupling (SOC) is taken into account. The *k*-point grid in the self-consistent process was $11 \times 11 \times 11$. To get the tight-binding model Hamiltonian, we used the package *wannier90* to obtain maximally localized Wannier functions (MLWFs)[34] of Mo *d* orbitals and P *p* orbitals. The space group of MoP is $P\bar{6}m2$ (number 187). The lattice constants $a = b = 3.222$ Å and $c = 3.198$ Å, and the atomic sites, are in agreement with the experimental values.

**Data availability.** The data that support the findings of this study are available from the corresponding authors on reasonable request.

31. Strocov, V. N. *et al.* Soft-X-ray ARPES facility at the ADRESS beamline of the SLS: concepts, technical realisation and scientific applications. *J. Synchrotron Radiat.* **21,** 32–44 (2014).
32. Kresse, G. & Furthmüller, J. Efficient iterative schemes for *ab initio* total-energy calculations using a plane-wave basis set. *Phys. Rev. B* **54,** 11169–11186 (1996).
33. Perdew, J. P., Burke, K. & Ernzerhof, M. Generalized gradient approximation made simple. *Phys. Rev. Lett.* **77,** 3865–3868 (1996).
34. Marzari, N. & Vanderbilt, D. Maximally localized generalized Wannier functions for composite energy bands. *Phys. Rev. B* **56,** 12847–12865 (1997).